

Quantification of switchable thermal conductivity of ferroelectric materials through second-principles calculation



Jingtong Zhang^{a,1}, Chengwen Bin^{b,1}, Yunhong Zhao^a, Huazhang Zhang^c, Sheng Sun^a, Peng Han^b, Chang Liu^d, Tao Xu^{e,f}, Gang Tang^g, Tong-Yi Zhang^h, Jie Wang^{a,b,*}

^a Research Center of Intelligent Computing Platform, Zhejiang Laboratory, Hangzhou 311100, Zhejiang, China

^b Department of Engineering Mechanics, Zhejiang University, Hangzhou, 310027, Zhejiang, China

^c Theoretical Materials Physics, Q-MAT, CESAM, University de Liege, B-4000 Sart-Tilman, Belgium

^d School of Mechanical and Aerospace Engineering, Southwest Jiaotong University, Chengdu 610031, China

^e Ningbo Institute of Materials Technology and Engineering, Chinese Academy of Sciences, Ningbo 315201, China

^f Department of Mechanical Engineering and Science, Kyoto University, Nishikyo-ku, Kyoto 615-8540, Japan

^g Advanced Research Institute of Multidisciplinary Science, Beijing Institute of Technology, Beijing 100081, China

^h Guangzhou Municipal Key Laboratory of Materials Informatics, Advanced Materials Thrust and Sustainable Energy and Environment Thrust, Hong Kong University of Science and Technology (Guangzhou), Guangzhou 511400, China

ARTICLE INFO

Keywords:

Second-principles method
Thermal conductivity
Thermal switch
Ferroelectric materials
Barium titanate

ABSTRACT

Materials with tunable thermal properties at room temperature have attracted great attention owing to their applications as solid-state thermal switches for thermal management. As a typical ferroelectric material, barium titanate (BaTiO_3) is regarded as promising candidate for thermal switch because its ferroelectric polarization can be switched by external electric field. However, BaTiO_3 presents a low-symmetry tetragonal phase at room temperature, calculating its thermal conductivity through first-principles calculations is rather time-consuming. By solving Boltzmann transport equation with the interatomic force constants from second-principles model, we develop a time-efficient strategy to calculate the thermal conductivity of tetragonal BaTiO_3 . The calculated thermal properties of BaTiO_3 based on the strategy are consistent with those from first-principles calculations while the calculation time is greatly reduced. It is found that both in-plane and out-of-plane thermal conductivity can be adjusted by external electric field. A thermal switch with a switch ratio of 5.1 at room temperature is predicted based on the polarization switching under external electric field. This work not only provides an efficient approach to study thermal properties but also suggests a room-temperature thermal switch controlled by an electric field.

1. Introduction

A thermal switch is a device that can control heat transfer through adjustment of its thermal conductivity [1,2]. It has attracted much attention due to its potential applications in solid-state refrigeration and electronic devices [3–6]. Thermal switches can exhibit the ‘on’ and ‘off’ states of thermal conductivity. The ‘on’ state is accompanied with a high thermal conductivity, while the ‘off’ state represents a small thermal conductivity. The ratio of the thermal conductivity between the two states is called ‘switching ratio’, which is used to evaluate the performance of thermal switches. Traditional thermal switches are liquid-based or gap-based [7–11], their switching ratio can reach as high

as 2000 [12]. However, the complicated mechanical structures of these thermal switches limit their further applications.

Solid-state thermal switches, whose thermal conductivity can be simply varied without complex mechanical structures, have gained much attention in recent years. Comparing to traditional mechanical switches, the solid-state thermal switches are more reliable [13], easier to miniaturize [14–16], and have faster response [17–19]. Constructing a solid-state thermal switch requires that the thermal conductivity of the material changes when it is triggered. Different trigger mechanisms have been discovered, such as temperature, electric fields, magnetic fields, light, and strain [13,19–25]. Among them, electric field triggered thermal switches are highly efficient and are often realized by

* Corresponding author. Research Center of Intelligent Computing Platform, Zhejiang Laboratory, Hangzhou 311100, Zhejiang, China.

E-mail address: jw@zju.edu.cn (J. Wang).

¹ Jingtong Zhang and Chengwen Bin contributes equally to this work.

ferroelectric materials, in which the thermal conductivity can be tuned via domain evolution or ferroelectric polarization switching [26–28]. The first ferroelectric thermal switch dates back to 2015 when Foley et al. [29] built a thermal switch based on $\text{PbZr}_{0.3}\text{Ti}_{0.7}\text{O}_3$ thin film. At room temperature, they observed that the thermal conductivity increased from $1.42 \text{ W m}^{-1} \text{ K}^{-1}$ to $1.61 \text{ W m}^{-1} \text{ K}^{-1}$ with the application of external electric field. Since then, several experimental studies on electric field triggered thermal switching in ferroelectric materials have been carried out. Ning et al. suggested that the thermal properties of BiFeO_3 can be controlled through different domain structures [30]. Langenberg et al. found that a domain wall can cause a 61 % reduction of the room-temperature thermal conductivity in PbTiO_3 thin films [27]. Recently, the phase transitions of PbZrO_3 were used to build a thermal switch with a 38 % switching ratio by Aryana et al. [31]. These works guarantee ferroelectric materials as promising candidates for thermal switches. Simultaneously, some theoretical studies have also been conducted on thermal switches of ferroelectric materials [32–36]. In 2018, Liu et al. investigated the thermal conductivity of BaTiO_3 under different electric fields [37]. A theoretical maximum thermal conductivity switching ratio of 9.4 was found in BaTiO_3 at 400 K under an electric field of 260 MV/m. However, their study focused on the order-disorder phase transition occurring above the Curie temperature (398 K) of BaTiO_3 . Since BaTiO_3 presents a tetragonal phase at room temperature, it is crucial to understand its thermal conductivity at room temperature.

In order to elucidate thermal conductivity of the tetragonal phase of BaTiO_3 , the thermal conductivity can be investigated by solving the linearized Boltzmann transport equation with interatomic force constants (IFCs) from first-principles calculations. The IFCs are obtained from supercell-based finite displacement difference method, which is rather time consuming due to the huge number of computation tasks using large supercell. For example, a system of $2 \times 2 \times 2$ supercell with 5 atoms per unit cell, the number of calculations is $4 \times 9 \times 2 \times 2 \times 2 \times 5^2$ [38]. Although this number can be reduced through symmetry or some other strategy [39], it's still a hard task to perform so huge number of computational tasks, especially on low-symmetry structures. To overcome this time-consuming problem, an alternative method is to construct an accurate effective potential, such as (semi)empirical potentials or machine-learned potentials (MLPs), which are employed to solve the Boltzmann transport equation with IFCs [40–43]. However, (semi)empirical potentials usually do not offer sufficient accuracy [44], while accurate MLPs are hard to be trained, since the dataset of MLPs typically requires 2000–12000 structures [45,46].

The limitation of above methods can be overcome to some extent by second-principles method. Second-principles method construct an atomic model based on a Taylor expansion of the potential energy surface around a reference structure [47]. Generally, the high symmetry cubic phase is selected as reference structure. By making full use of the phonon dispersion of the reference structure calculated from DFT, the potentials obtained from second-principles method are much more accurate than (semi)empirical potentials. The concise mathematical expression used in this method makes it much more efficient than MLPs. Several successful second-principles models have been built for NdNiO_2 , CaTiO_3 , PbTiO_3 , SrTiO_3 and PTO/STO superlattices. These models have subsequently been used to study phase transition [48,49], negative capacitance [50], polar skyrmions [51], and energy storage [52,53]. The above works prove the effectiveness of the second-principles method and make us wonder whether the second-principles method is suitable for studying the heat transfer properties in ferroelectric materials.

In this work, a second-principles model for BaTiO_3 is constructed. The lattice thermal conductivity of BaTiO_3 is studied by solving the Boltzmann transport equation with IFCs calculated from the second-principles model. After validating the effectiveness of this model, we investigate the thermal conductivity of tetragonal BaTiO_3 at room temperature. The calculated thermal properties of BaTiO_3 are consistent with those from first-principles calculations. A large difference between the in-plane and out-of-plane thermal conductivity in tetragonal BaTiO_3

is found. This difference makes it possible to construct thermal switch based on ferroelectric polarization switching. After applying external electric field, both in-plane and out-of-plane thermal conductivity can be adjusted. The switching ratio can be enhanced up to 5.1 at room temperature. This work not only provides an efficient approach to study thermal conductivity at the atomic level but also suggests the potential of BaTiO_3 as an electric field controlled thermal switch at room temperature.

2. Methodology

2.1. First-principles calculation

First-principles calculations are performed using the Vienna ab initio simulation package (VASP) based on density functional theory [54,55]. PBEsol is used as the electron exchange-correlation potential [56], and the plane-wave cutoff is 600 eV. The valence electrons of Ba ($5s^2 5p^6 6s^2$), Ti ($3s^2 3p^6 3d^2 4s^2$), and O ($2s^2 2p^4$) are used. The crystal structure is fully relaxed until the Hellmann-Feynman forces on each atom were converged to less than $10^{-3} \text{ eV}/\text{\AA}$. The Brillouin zone is sampled by using an $8 \times 8 \times 8$ Monkhorst-Pack k-point mesh for structure relaxations. The phonon dispersions are computed using the *Phonopy* program package [57], in which a linear response method based on density functional perturbation theory (DFPT) is employed [58]. The phonon dispersion is obtained using a $2 \times 2 \times 2$ supercell with a $4 \times 4 \times 4$ k-point mesh.

2.2. Second-principles method

The second-principles method describes the potential energy surface with a Taylor expansion around a reference structure. In this work, we selected cubic phase of BaTiO_3 as reference structure. The total energy can be described as [47]:

$$E^{tot} = E_p\{u_i\} + E_s\{\eta\} + E_{s-p}\{u_i, \eta\} \quad (1)$$

where E_p is the energy from atom displacements, E_s is the elastic energy, and E_{s-p} is the coupling between strain and atom displacements. Through Taylor expansion, Eq. (1) can be expanded as a function of displacement and strain (see Supporting Information). The harmonic terms of this model are directly obtained from phonons of cubic structure. The anharmonic terms are fitted by the training sets calculated from first-principles. The training set include 1491 structures, which are generated from the linear interpolation between all the unstable modes of the cubic phase. Since the harmonic terms are directly computed from DFT calculations, second-principles model is physics involved and required less training data than MLPs. Comparing to the 5100 structures required in MLPs for BaTiO_3 [59], this training set of 1491 structures is much smaller. The energies and forces of these structures are calculated with the *Abinit* package [60,61]. After the energies and forces of each training set structure are obtained, the fitting procedure is carried out with the software package *Multibinit*, which is released within the *Abinit* package. During the fitting procedure, the cutoff for short interactions is selected as 4.1 Å, and 24 anharmonic terms are chosen. The final convergence value of the goal function with respect to forces is $7.896 \times 10^{-5} \text{ eV}^2/\text{\AA}^2$, which is much better than that for the second-principles model of SrTiO_3 [62]. All the anharmonic terms and their parameters are listed in Table S1.

2.3. Thermal conductivity

Thermal conductivities are obtained by solving the phonon Boltzmann transport equation using the *Phono3py* software package [63,64]. The lattice thermal conductivity κ at temperature T is given by Ref. [65]:

$$\kappa_l^{\alpha\beta} = \frac{\hbar^2}{k_B T^2 N \Omega} \sum_{\lambda} f_0 (f_0 + 1) (\omega_{\lambda})^2 v_{\lambda}^{\alpha} v_{\lambda}^{\beta} \tau_{\lambda} \quad (2)$$

where k_B is the Boltzmann constant, N is the number of k points, Ω is the volume of the unit cell, and f_0 is the Bose–Einstein statistics. v_{λ}^{α} and v_{λ}^{β} are the components of the group velocity, and τ_{λ} is the phonon lifetime. The group velocity and phonon lifetime are determined by the IFCs. Supercell-based finite displacement difference method is carried out to obtain IFCs. After generating thousands of structures with *Phono3py*, the forces on each atom in these structures are calculated with second-principles method. The harmonic second-order IFCs and third-order IFCs are calculated using $3 \times 3 \times 3$ supercell corresponding to a lattice parameter of 12 Å. After testing convergence of \mathbf{q} points mesh, $21 \times 21 \times 21$ \mathbf{q} points are used in the calculations.

3. Results and discussion

3.1. Accuracy of the second-principles model

3.1.1. Model testing

In this work, the second-principles model is obtained by using a least-square fitting procedure that includes a training set of 1491 structures. The accuracy of the fitting procedure is firstly examined by comparing the energies and forces from the DFT and the second-principles model for the training set. A comparison of the energies and stresses is shown in Fig. 1. Additional 220 structures are employed as testing set to test the second-principles model. The energies calculated from second-principles model are compared with those from the DFT for the testing set, which are shown in Fig. S1. All the points in Fig. 1 and S1 are close to the straight-line $x = y$, indicating that the accuracy of the second-

principles model is excellent.

3.1.2. Comparison on the tetragonal phase

Next, we focus on the tetragonal structure of BaTiO₃ presented by the second-principles model. At room temperature, BaTiO₃ exhibits a tetragonal structure in which the atoms have relative displacements along the z-direction, as shown in Fig. 2 (a) and (b). We simulate the tetragonal phase of BaTiO₃ with the second-principles model and compare the results with DFT and experimental results. As shown in Table 1, the lattice constants from the second-principles model agree well with the experimental results. The distortion of the Ti atom, which is the main reason for the ferroelectricity in BaTiO₃, is very close to the experimental result. Furthermore, we calculate the phonon dispersion at zero temperature, by using the second-principles model and first-principles calculations, and show the result in Fig. 2 (c). The phonon dispersions from the second-principles model and DFT coincide quite well. Fig. 2 (d) gives the projected density of states (PDOS) of tetragonal BaTiO₃. It is found that the acoustic phonons are mainly contributed by the Ba atoms, while optical phonons are contributed by Ti and O atoms. Moreover, the imaginary modes make an almost negligible contribution to the PDOS, suggesting that their contribution to the thermal properties can be ignored, which is similar to that in Cmcm SnSe [66]. An optical-optical gap occurs in the frequency range of 540–670 cm⁻¹ and the optical phonon branches with larger frequency are only contributed by O atoms. The general dispersion, band gaps and widths are well reproduced by the second-principles model. Notably, the highest energy band also consistent with the DFT results. This congruence suggests the viability of the second-principles model for studying the thermal properties of BaTiO₃.

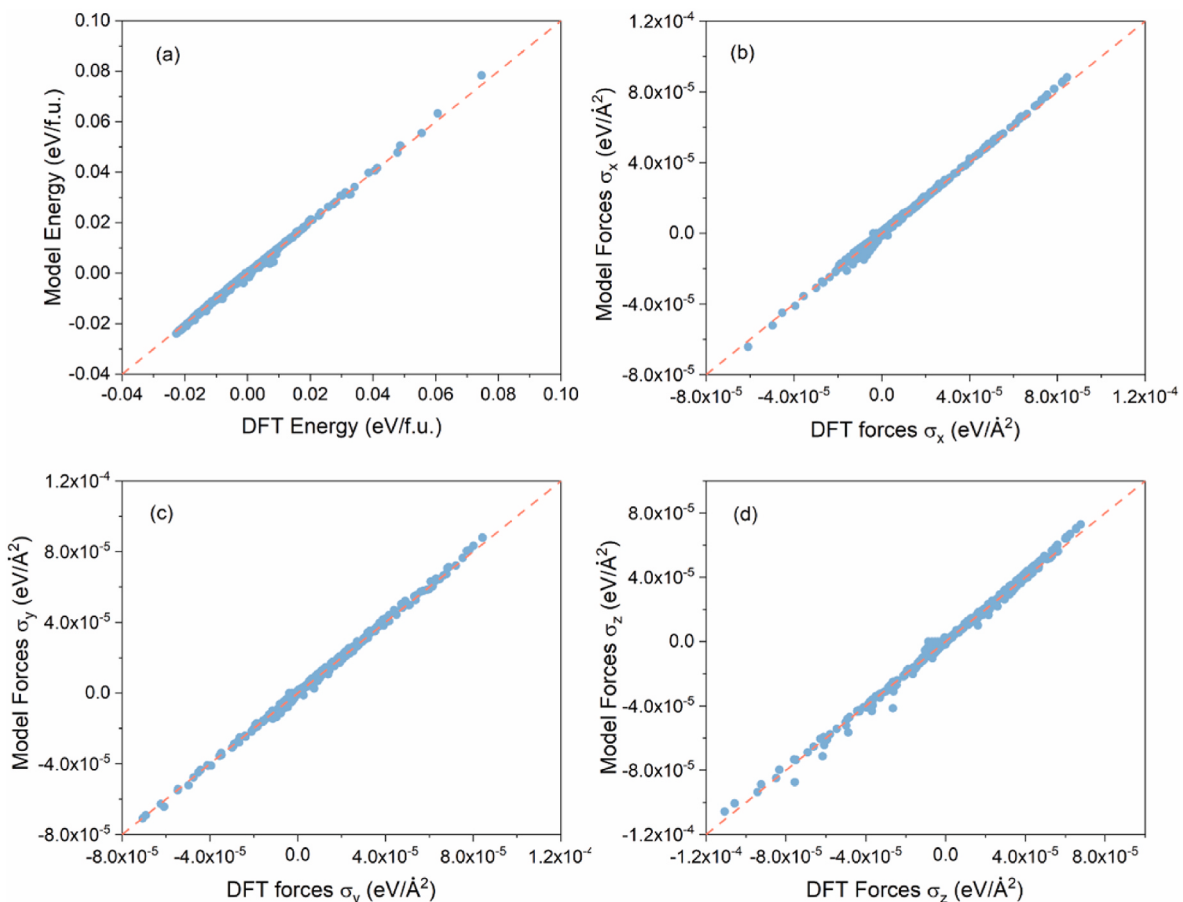


Fig. 1. (a) Comparison of energies and (b–d) forces from the second principle model and DFT calculations for the training set.

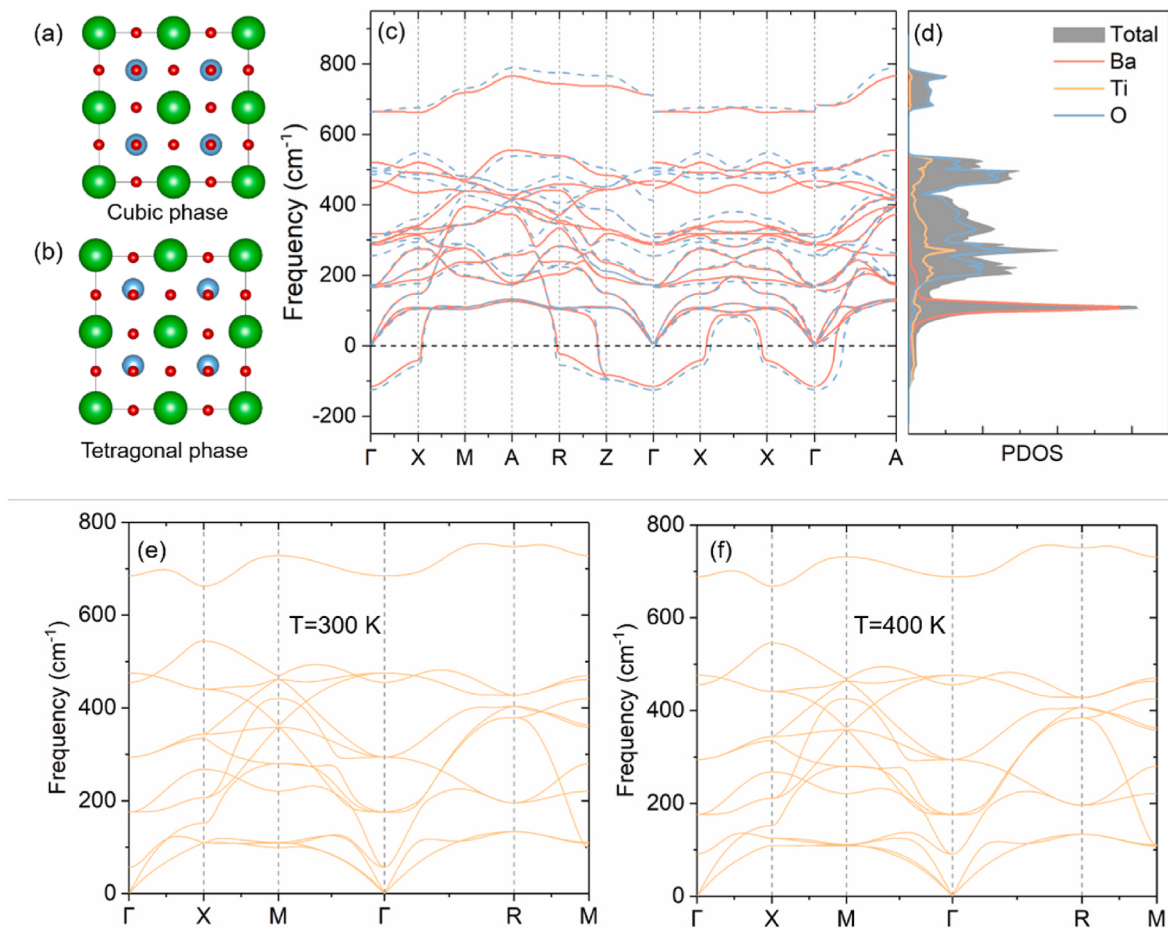


Fig. 2. Structure of the (a) cubic and (b) tetragonal phases of BTO. (c) Phonon dispersion and (d) projected density of states (PDOS) of tetragonal BTO at zero temperature. The dashed lines and PDOS are calculated by the second-principles method, while the solid lines are obtained via DFT calculations. Finite temperature phonon dispersion calculated by second-principles method at (e) 300 K and (f) 400 K.

Table 1
Structure parameters of tetragonal BaTiO₃ from experiments, DFT calculations and the second-principles method.

Tetragonal BaTiO ₃ (Space Group: P4mm)			
Ref. [67] (exp. at 280 K)	Ref. [68] (DFT with PBE)	Ref. [69] (DFT with LDA)	This work
a = b = 3.9970 (Å)	a = b = 3.976 (Å)	a = b = 3.994 (Å)	a = b = 3.985 (Å)
c = 4.032 (Å)	c = 4.172 (Å)	c = 4.036 (Å)	c = 4.050 (Å)
V = 64.406 (Å ³)	V = 65.9533 (Å ³)	V = 64.382 (Å ³)	V = 64.315 (Å ³)
c/a = 1.009	c/a = 1.050	c/a = 1.011	c/a = 1.016
Displacements (Å)			
Ba 0.0	Ba 0.0	Ba 0.0	Ba 0.0
Ti 0.08183	Ti 0.078433	Ti 0.05771	Ti 0.06438
O1 -0.04958	O1 -0.11097	O1 -0.07506	O1 -0.0144
O2 -0.04958	O2 -0.11097	O2 -0.07506	O2 -0.0144
O3 -0.1040	O3 -0.197335	O3 -0.1239	O3 -0.0616

3.1.3. Comparison on the thermal conductivity

The thermal properties of the high-symmetry cubic phase of BaTiO₃ are calculated by 220 self-consistent runs of first-principles calculations and the results are compared with the results from the second-principles model. As shown in Fig. 3 (a), the thermal conductivity approximately follows the T^{-1} relationship, decreasing with an increasing temperature. Although the second-principles model presents slightly larger results than DFT, the trends of the two curves agree well with each other. The difference originates from the fact that the software packages used to generate the second-principles model differ from that used to calculate

the thermal conductivity from DFT. Next, we calculate the thermal conductivity of rhombohedral (the ground state) BaTiO₃, and compare it with the results in the literature [37]. As shown in Fig. 3 (b), it is clear that the results calculated by the second-principles model are almost identical to those in the literature. The above results combined with ultra-short computation time (only a few minutes), indicating that the second-principles model is efficient and accurate in studying the thermal conductivity of BaTiO₃.

3.2. Thermal conductivity of tetragonal BaTiO₃

After the verification of the second-principles model, we focused on the thermal properties of BaTiO₃ at room temperature. Since BaTiO₃ presents a tetragonal phase at room temperature, we studied the thermal conductivity of tetragonal BaTiO₃ with the second-principles model.

Fig. 4 (a) shows the specific heat of tetragonal BaTiO₃ as a function of temperature T . The variation rate of the specific heat at low temperature is much larger than that of high temperature, which exhibits the general thermal properties of a solid material. Fig. 4 (b) shows the calculated lattice thermal conductivity of tetragonal BaTiO₃ perpendicular (κ_{in}) or parallel (κ_{out}) to the direction of polarization as a function of temperature. At room temperature (300 K), the value of κ_{in} is $2.11 \text{ W m}^{-1}\text{K}^{-1}$, while the κ_{out} is only $1.65 \text{ W m}^{-1}\text{K}^{-1}$. The thermal conductivity calculated here only include particle-like component, while the wave-like thermal conductivity component are ignored. Given that wave-like contributions to thermal conductivity are typically expected in crystalline solids with larger unit cells [24] or extremely low thermal

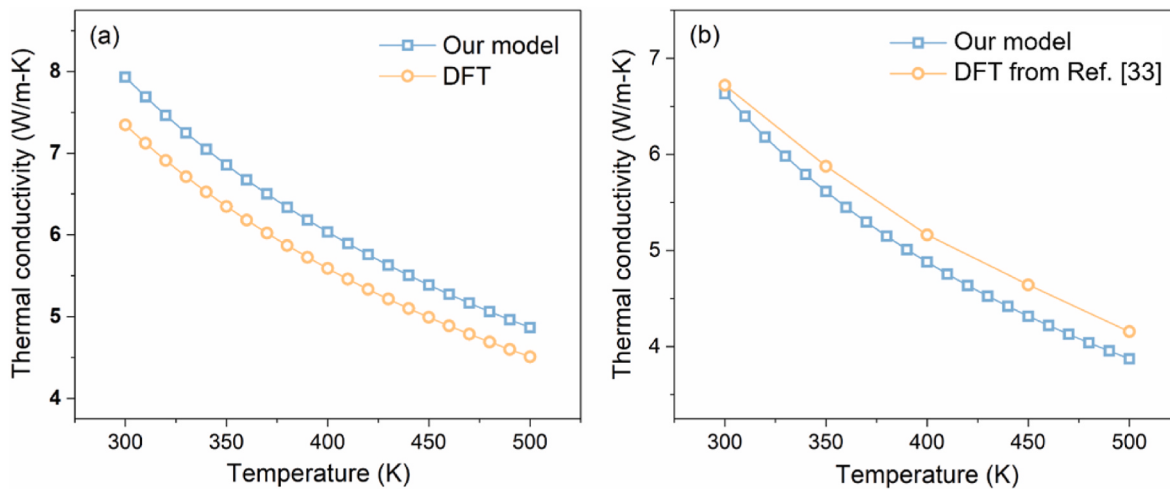


Fig. 3. Comparison of the thermal conductivities of the cubic phase (a) and rhombohedral phase (b) of BaTiO₃. The thermal conductivities of the cubic phase are calculated based on a $3 \times 3 \times 3$ supercell, and the DFT results of the rhombohedral phase come from Ref. [37].

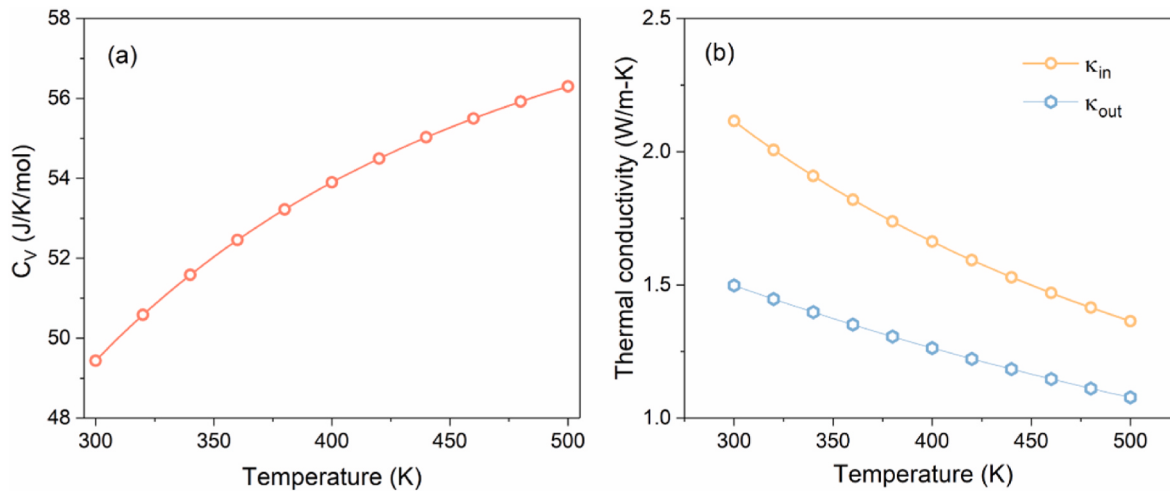


Fig. 4. (a) The variation of the specific heat of tetragonal BaTiO₃ lattice as a function of temperature. (b) The variation of the thermal conductivity of tetragonal BaTiO₃ lattice as a function of temperature. The solid and dashed lines are the thermal conductivities perpendicular and parallel to the direction of polarization, respectively.

conductivity [70], their impact on the thermal conductivity of tetragonal BaTiO₃ is considered negligible. Fig. S4 gives the total thermal conductivity and contribution from particle-like component and wave-like component. The difference between κ_{in} and κ_{out} suggests an intrinsic anisotropy of the thermal conductivity in tetragonal BaTiO₃, which can be used to design solid-state thermal switches by modifying the direction of polarization.

Furthermore, we analyzed the frequency dependence and mean free path dependence of the cumulative κ_{in} and κ_{out} at room temperature for BaTiO₃. As shown in Fig. 5 (a), the thermal conductivity perpendicular to the polarization is influenced by acoustic phonons to the extent of 46 %, whereas their contribution is comparatively lower at 34 % in the parallel direction. Moreover, the contribution from optical phonons to the in-plane thermal conductivity mainly accumulates in the range of 200 cm⁻¹ to 400 cm⁻¹, which indicates that low-frequency optical phonons dominate the in-plane heat carriers. Meanwhile, the contribution from optical phonons to the out-of-plane thermal conductivity is distributed across each frequency. The differences between the in-plane and out-of-plane thermal conductivity as a function of frequency are summarized in Fig. 5 (c). The difference between κ_{in} and κ_{out} increases at low frequencies but decreases at high frequencies. The increasing

between κ_{in} and κ_{out} at low frequencies originates from a larger in-plane phonon group velocity. As is shown in Fig. 2 (b), the slope of phonon branches in the frequency range 100–300 cm⁻¹ from X to M is larger than that from Γ to Z indicating a relatively higher in-plane phonon group velocity. Fig. 5 (b) shows the cumulative κ_{in} and κ_{out} versus phonon mean free path. Most of the thermal conductivities are contributed by phonons with a mean free path shorter than 10 nm, which is similar to the disordered structure of BaTiO₃, indicating a strong phonon scattering in tetragonal BaTiO₃.

3.3. Room temperature electric field controlled thermal switch

The polarization in ferroelectric materials can be adjusted by an external electric field, and this process is usually accompanied with alterations in thermal conductivity. This property makes ferroelectric materials potential candidates for thermal switch. The utilization of second-principles method in this work could significantly reduce computation costs, and enable the study of the thermal properties pertaining to low-symmetry structures generated by different electric fields at room temperature. We started with a simpler case in which the electric field is applied along the direction of polarization. Under the

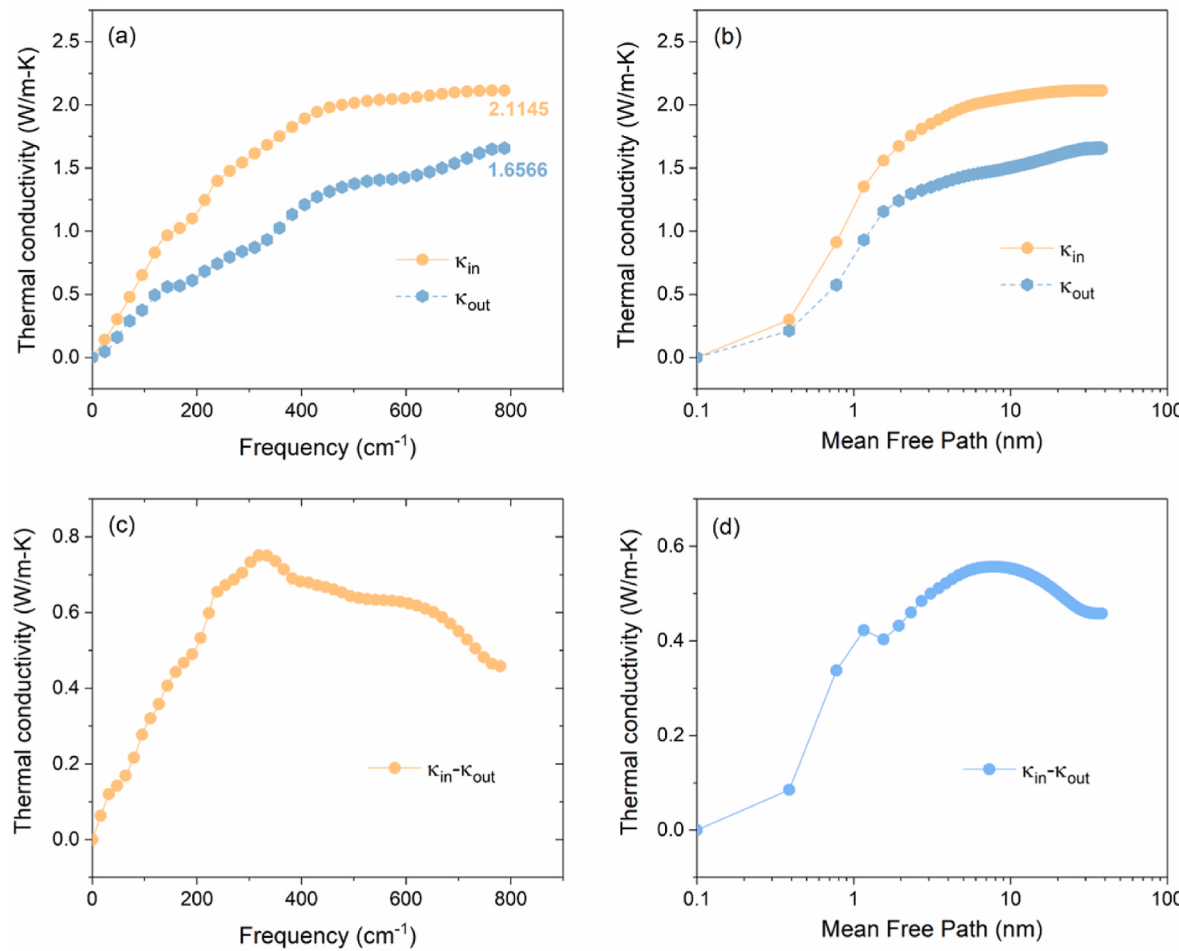


Fig. 5. (a) Frequency dependence and (b) mean free path dependence of the cumulative thermal conductivity at 300 K for tetragonal BTO. The solid and dashed lines are the thermal conductivities perpendicular and parallel to the direction of polarization, respectively. Difference between the cumulative κ_{in} and κ_{out} as a function of (c) frequency and (d) mean free path.

[001] electric field, the structure remains in the tetragonal phase. Fig. 6 (a) shows the changes in the polarization of tetragonal BaTiO₃ with the electric field. The spontaneous polarization at zero field is 0.38 C/m², which is much larger than that from the experiment (0.26 C/m² at 300 K) [71]. This is due to the fact that our simulation was carried out at zero

temperature and neglected the influences of temperature. The dependences of the κ_{in} and κ_{out} at 300 K on the applied electric field are presented in Fig. 6 (b). Although the electric field has little influence on the out-of-plane thermal conductivity, the in-plane thermal conductivity significantly increases at -30 kV/cm. The switching ratio, which is an

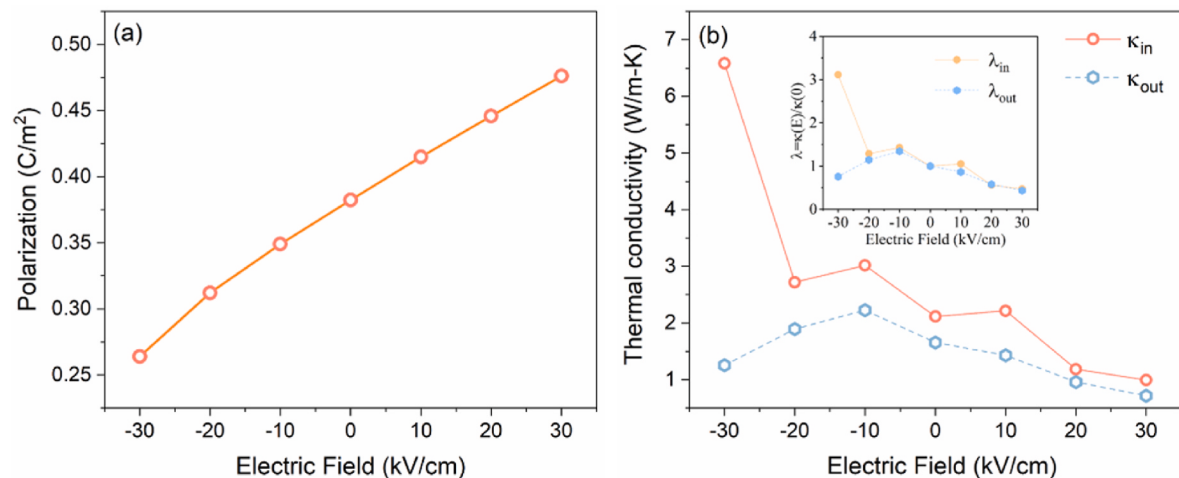


Fig. 6. (a) Changes in the polarization of tetragonal BaTiO₃ with electric field. The electric field is applied parallel to the polarization and is much smaller than the coercive electric field. The positive electric field represents that it is in the same direction as the polarization, while negative one represents an opposite direction. (b) Changes in the thermal conductivity of tetragonal BaTiO₃ with electric field. The insert is the switch ratio induced by the electric field.

important indicator for evaluating thermal switches, is calculated by $\lambda = \kappa(E)/\kappa(0)$, where $\kappa(E)$ is the thermal conductivity under an external electric field, while $\kappa(0)$ is the thermal conductivity without electric field. The switching ratios under different electric fields are shown in the insert of Fig. 6 (b). The 3.11-fold increase under the electric field of -30 kV/cm suggests the potential of using BaTiO₃ for thermal switch applications. To understand the effects of the electric field on the thermal conductivity, we plotted the cumulative κ_{in} and κ_{out} versus frequency and phonon mean free path in Fig. 7 (a) and (b), respectively. According to Fig. 7, the electric field can significantly enhance the heat transfer capability of the acoustic and low-frequency optical branches. This indicates that we should focus on the low-frequency phonon branches to understand the mechanism of enhancement in thermal conductivity from electric field. Thus, we calculated phonons of BaTiO₃ at -30 kV/cm and compared it with that without electric field. As is shown in Fig. S3, the frequency at X point changes from negative to positive and causes an enhancement of in-plane thermal conductivity. The negative frequency in the phonons indicates a phonon instability. Since the phonon instabilities are localized to regions of infinitesimal volume in reciprocal space, they do not participate in thermal properties [66]. Stabilizing an instability phonon mode through electric field can make this phonon branch contribute to the thermal conductivity. This result suggests a different mechanism of electric field enhancement in thermal conductivity from that in Ref. [37].

Next, we investigated the effects of an electric field perpendicular to the direction of polarization. This electric field can align polarization vectors from [001] to [100]. A thermal switch can be built due to the difference between κ_{in} and κ_{out} . Due to the computational cost arising from the absence of symmetry in the structure during polarization realignment, the calculation of thermal conductivity through first-principles approach becomes unfeasible. However, the second-principles method used in this work enables this calculation so that we can investigate this process. After applying electric field on [100] direction, the direction of polarization rotates from [001] to [100] gradually. We captured the structures during this process and calculated their thermal conductivities with second-principles model. The changes in the thermal conductivity with the direction of polarization are shown in Fig. 8 (a). The switching ratio shown in Fig. 8 (b) is defined by $\lambda = \kappa_{xx}/\kappa_{zz}$. Although the maximum switching ratio is 1.43, which is smaller than that when the electric field is applied along the [001] direction, this work proves the feasibility that a thermal switch can be constructed through the anisotropic thermal conductivity exhibited by BaTiO₃.

Finally, we concluded two main characteristics of tetragonal BaTiO₃ from the thermal conductivity analysis presented in the above results.

First, the thermal conductivity of BaTiO₃ is anisotropic, and the difference between κ_{in} and κ_{out} can be adjusted by an electric field along the direction of ferroelectric polarization. Second, the direction of ferroelectric polarization can be realigned by an electric field. Combining the above two factors, we can design the way of applying electric field to get the maximum switch ratio. We can firstly apply an electric field along the [001] direction and then converted to the [100] direction. In this way, an electric field-controlled room temperature thermal switch with a theoretical thermal conductivity switching ratio of 5.1 in ferroelectric BaTiO₃ is predicted.

4. Summary and conclusions

In summary, we have successfully constructed an atomistic second-principles model, based on which we have developed a new strategy to predict thermal conductivity of BaTiO₃. The reduced computational cost allows us to investigate the thermal properties of tetragonal BaTiO₃ at room temperature more efficiently. The validation of the model on structure and phonon demonstrated that the second-principles model is accurate enough to predict the thermal properties of BaTiO₃. The anisotropic thermal conductivity is found in tetragonal BaTiO₃. Both in-plane and out-of-plane thermal conductivity can be adjusted by external electric field. We investigate two ways for applying external electric field, which are along the direction of polarization and perpendicular to the direction of polarization, respectively. An electric field of -30 kV/cm along the direction of polarization can lead to a 3.11-fold increase of in-plane thermal conductivity. This result suggests the potential of using BaTiO₃ for thermal switch applications. Furthermore, the combination of two ways of applying electric field suggests a possible thermal conductivity switching ratio of 5.1 at room temperature. This work not only provides an accurate and accelerating method to study thermal conductivity at the atomic level but also predict a room-temperature thermal switch with a large thermal conductivity switching ratio.

CRediT authorship contribution statement

Jingtong Zhang: Writing – review & editing, Writing – original draft, Visualization, Validation, Software, Resources, Project administration, Methodology, Investigation, Formal analysis, Data curation, Conceptualization. **Chengwen Bin:** Writing – review & editing, Formal analysis, Conceptualization. **Yunhong Zhao:** Writing – review & editing, Validation, Methodology, Investigation, Conceptualization. **Huazhang Zhang:** Data curation, Writing – review & editing. **Sheng Sun:** Supervision. **Peng Han:** Writing – review & editing, Visualization,

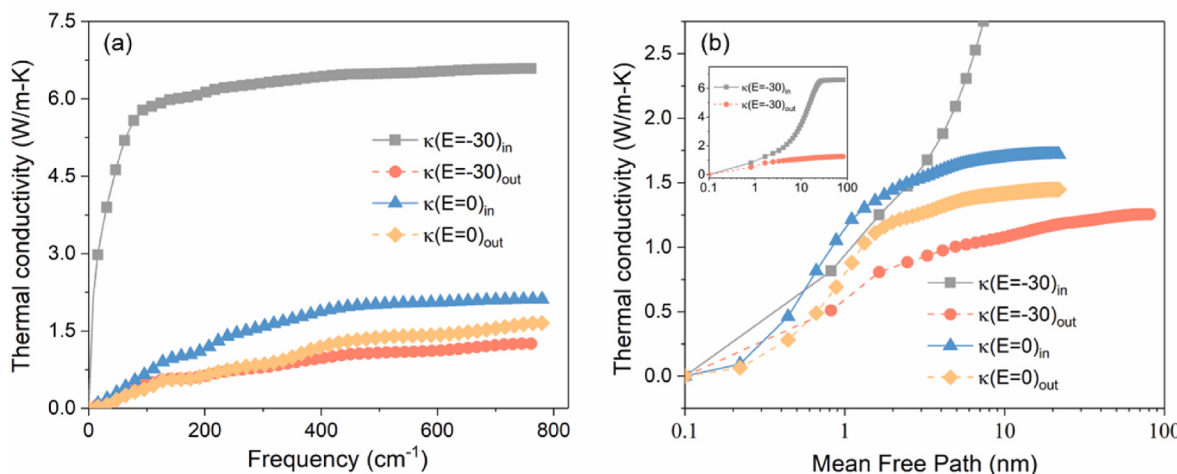


Fig. 7. (a) Frequency dependence and (b) mean free path dependence of the cumulative thermal conductivity at 300 K for BTO under different electric fields. The solid and dashed lines are the thermal conductivities perpendicular and parallel to the direction of polarization, respectively.

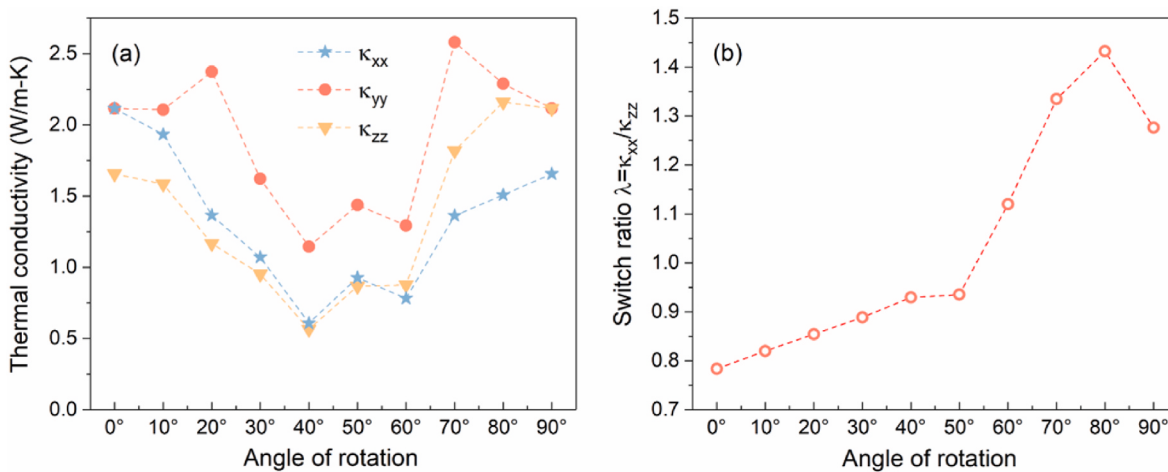


Fig. 8. (a) Variation of the thermal conductivity with the direction of polarization. (b) The switch ratio between the thermal conductivities in the [100] and [001] directions.

Validation, Investigation. **Chang Liu:** Resources, Investigation. **Tao Xu:** Writing – review & editing, Validation, Methodology, Investigation, Conceptualization. **Gang Tang:** Validation, Software, Methodology, Investigation, Conceptualization. **Tong-Yi Zhang:** Writing – review & editing, Validation, Supervision. **Jie Wang:** Writing – review & editing, Validation, Supervision, Methodology, Investigation, Funding acquisition, Formal analysis, Conceptualization.

Declaration of competing interest

The authors declare that they have no known competing financial interests or personal relationships that could have appeared to influence the work reported in this paper.

Data availability

Data will be made available on request.

Acknowledgments

This work was supported by the National Program on Key Basic Research Project (Grant No.2022YFB3807601), National Natural Science Foundation of China (Grant No. 12272338, 12192214 and 12302208), Key Research Project of Zhejiang Laboratory (No. 2021PE0AC02) and Zhejiang Lab Research Initiation Project (No. K2022PE0PI02).

Appendix A. Supplementary data

Supplementary data to this article can be found online at <https://doi.org/10.1016/j.mtphys.2024.101347>.

References

- [1] P. Ben-Abdallah, S.-A. Biehs, Near-field thermal transistor, *Phys. Rev. Lett.* 112 (2014) 044301.
- [2] J.-H. Cho, T.S. Wiser, C.D. Richards, D.F. Bahr, R.F.J.S. Richards, A. A-physical, Fabrication and characterization of a thermal switch, *Sensors and Actuators A-physical* 133 (2007) 55–63.
- [3] Y. Utaka, K. Hu, Z. Chen, Y. Zhao, Application of simple and effective thermal switch for solid-state magnetic refrigeration at room temperature, *Appl. Therm. Eng.* 155 (2019) 196–205.
- [4] K. Klinar, A. Kitanovski, Thermal control elements for caloric energy conversion, *Renew. Sustain. Energy Rev.* 118 (2020) 109571.
- [5] P.K. Schelling, L. Shi, K.E. Goodson, Managing heat for electronics, *Mater. Today* 8 (2005) 30–35.
- [6] G. Wehmeyer, T. Yabuki, C. Monachon, J. Wu, C. Dames, Thermal diodes, regulators, and switches: physical mechanisms and potential applications, *Appl. Phys. Rev.* 4 (2017).
- [7] J. Cho, C. Richards, D. Bahr, J. Jiao, R. Richards, Evaluation of contacts for a MEMS thermal switch, *J. Micromech. Microeng.* 18 (2008) 105012.
- [8] M. Leriche, S. Harmand, M. Lippert, B.J.A.T.E. Desmet, An experimental and analytical study of a variable conductance heat pipe: application to vehicle thermal management, *Appl. Therm. Eng.* 38 (2012) 48–57.
- [9] R. Prasher, Thermal interface materials: historical perspective, status, and future directions, *Proc. IEEE* 94 (2006) 1571–1586.
- [10] I.S. McKay, E.N. Wang, Pulsed Heat Transfer for Thermal Maximum Power Point Tracking, ASME 2013 International Mechanical Engineering Congress and Exposition, 2013.
- [11] Y. Jia, Y.S. Ju, Solid-liquid hybrid thermal interfaces for low-contact pressure thermal switching, *J. Heat Tran.* 136 (2014).
- [12] M. Westwood, M. S. thesis, University of California, Berkeley, (2015). DOI.
- [13] T. Swoboda, K. Klinar, A.S. Yalamarthi, A. Kitanovski, M. Muñoz Rojo, Solid-state thermal control devices, *Advanced Electronic Materials* 7 (2021): 200625.
- [14] C.Y. Tsou, C.Y.H. Chao, Solid-state thermal diode with shape memory alloys, *Int. J. Heat Mass Tran.* 93 (2016) 605–611.
- [15] C. Acar, I. Dincer, Better thermal management options with heat storage systems for various applications: an Evaluation, *Energy Storage* 1 (2019) e47.
- [16] T. Luo, G. Chen, Nanoscale heat transfer – from computation to experiment, *Phys. Chem. Chem. Phys.* 15 (2013) 3389–3412.
- [17] Y. Lu, J. Jiang, W.H. Ki, A multiphase switched-capacitor DC-DC converter ring with fast transient response and small ripple, *IEEE J. Solid State Circ.* 52 (2017) 579–591.
- [18] M. Nomura, J. Shioimi, T. Shiga, R. Anufriev, Thermal phonon engineering by tailored nanostructures, *Jpn. J. Appl. Phys.* 57 (2018): 080101.
- [19] B.M. Foley, M. Wallace, J.T. Gaskins, E.A. Paisley, R.L. Johnson-Wilke, J.W. Kim, P. J. Ryan, S. Trolier-McKinstry, P.E. Hopkins, J.F. Ihlefeld, Voltage-controlled bistable thermal conductivity in suspended ferroelectric thin-film membranes, *ACS Appl. Mater. Interfaces* 10 (2018) 25493–25501.
- [20] J.C. Wu, J.Y. Zhao, H.S. Xu, X.G. Liu, A.A. Taskin, Y. Ando, X. Zhao, X.F. Sun, Thermal conductivity of ferrimagnet GdBaMn205.0 single crystals, *AIP Adv.* 7 (2016).
- [21] C. McGuire, K. Sawchuk, A. Kavner, Measurements of thermal conductivity across the B1-B2 phase transition in NaCl, *J. Appl. Phys.* 124 (2018).
- [22] X. Xu, J. Chen, J. Zhou, B. Li, Thermal conductivity of polymers and their nanocomposites, *Adv. Mater.* 30 (2018): 1705544.
- [23] S. Li, X. Ding, J. Ren, X. Moya, J. Li, J. Sun, E.K. Salje, Strain-controlled thermal conductivity in ferroic twinned films, *Sci. Rep.* 4 (2014) 6375.
- [24] Z. Tong, T. Dumitrică, T. Frauenheim, Intrinsically low thermal conductivity in the most lithium-rich binary stannide crystalline Li₅Sn, *J. Phys. Chem. Lett.* 14 (2023) 8139–8144.
- [25] Y. Zhang, T. Frauenheim, T. Dumitrică, Z. Tong, Theoretical insights into thermal conductivity variations in various phases of the Cu₂Te multiphase transition material, *ACS Appl. Energy Mater.* 6 (2023) 9657–9662.
- [26] D. Dangić, O. Hellman, S. Fahy, I. Savić, The origin of the lattice thermal conductivity enhancement at the ferroelectric phase transition in GeTe, *npj Comput. Mater.* 7 (2021) 57.
- [27] E. Langenberg, D. Saha, M.E. Holtz, J.-J. Wang, D. Bugallo, E. Ferreiro-Vila, H. Paik, I. Hanke, S. Ganschow, D.A. Muller, L.-Q. Chen, G. Catalan, N. Domingo, J. Malen, D.G. Schlom, F. Rivedulla, Ferroelectric domain walls in PbTiO₃ are effective regulators of heat flow at room temperature, *Nano Lett.* 19 (2019) 7901–7907.
- [28] C. Liu, P. Lu, Z. Gu, J. Yang, Y. Chen, Bidirectional tuning of thermal conductivity in ferroelectric materials using E-controlled hysteresis characteristic property, *J. Phys. Chem. C* 124 (2020) 26144–26152.

- [29] J.F. Ihlefeld, B.M. Foley, D.A. Scrymgeour, J.R. Michael, B.B. McKenzie, D. L. Medlin, M. Wallace, S. Trolier-McKinstry, P.E. Hopkins, Room-temperature voltage tunable phonon thermal conductivity via reconfigurable interfaces in ferroelectric thin films, *Nano Lett.* 15 (2015) 1791–1795.
- [30] S. Ning, S.C. Huberman, C. Zhang, Z. Zhang, G. Chen, C.A. Ross, Dependence of the thermal conductivity of BiFeO₃ thin films on polarization and structure, *Phys. Rev. Appl.* 8 (2017) 054049.
- [31] K. Aryana, J.A. Tomko, R. Gao, E.R. Hoglund, T. Mimura, S. Makarem, A. Salanova, M.S.B. Hoque, T.W. Pfeifer, D.H. Olson, J.L. Braun, J. Nag, J.C. Read, J.M. Howe, E. J. Opila, L.W. Martin, J.F. Ihlefeld, P.E. Hopkins, Observation of solid-state bidirectional thermal conductivity switching in antiferroelectric lead zirconate (PbZrO₃), *Nat. Commun.* 13 (2022) 1573.
- [32] C. Liu, Y. Chen, C. Dames, Electric-field-controlled thermal switch in ferroelectric materials using first-principles calculations and domain-wall engineering, *Phys. Rev. Appl.* 11 (2019) 044002.
- [33] D. Wei, E. Zhou, X. Zheng, H. Wang, C. Shen, H. Zhang, Z. Qin, G. Qin, Electric-controlled tunable thermal switch based on Janus monolayer MoS₂, *npj Comput. Mater.* 8 (2022) 260.
- [34] C. Liu, Z. Chen, C. Wu, J. Qi, M. Hao, P. Lu, Y. Chen, Large thermal conductivity switching in ferroelectrics by electric field-triggered crystal symmetry engineering, *ACS Appl. Mater. Interfaces* 14 (2022) 46716–46725.
- [35] J.A. Seijas-Bellido, H. Aramberri, J. Íñiguez, R. Rurrali, Electric control of the heat flux through electrophononic effects, *Phys. Rev. B* 97 (2018) 184306.
- [36] J.A. Seijas-Bellido, C. Escorihuela-Sayalero, M. Royo, M.P. Ljungberg, J.C. Wojdel, J. Íñiguez, R. Rurrali, A phononic switch based on ferroelectric domain walls, *Phys. Rev. B* 96 (2017) 140101.
- [37] C. Liu, V. Mishra, Y. Chen, C. Dames, Large thermal conductivity switch ratio in barium titanate under electric field through first-principles calculation, *Advanced Theory and Simulations* 1 (2018) 1800098.
- [38] W. Li, J. Carrete, N.A. Katcho, N. Mingo, ShengBTE, A solver of the Boltzmann transport equation for phonons, *Comput. Phys. Commun.* 185 (2014) 1747–1758.
- [39] G. Qin, M. Hu, Accelerating evaluation of converged lattice thermal conductivity, *npj Comput. Mater.* 4 (2018) 3.
- [40] H. Dong, C. Cao, P. Ying, Z. Fan, P. Qian, Y. Su, Anisotropic and high thermal conductivity in monolayer quasi-hexagonal fullerene: a comparative study against bulk phase fullerene, *Int. J. Heat Mass Tran.* 206 (2023) 123943.
- [41] Y.-B. Shi, Y.-Y. Chen, H. Wang, S. Cao, Y.-X. Zhu, M.-F. Chu, Z.-F. Shao, H.-K. Dong, P. Qian, Investigation of the mechanical and transport properties of InGeX₃ (X = S, Se and Te) monolayers using density functional theory and machine learning, *Phys. Chem. Chem. Phys.* 25 (2023) 13864–13876.
- [42] Y. Luo, M. Li, H. Yuan, H. Liu, Y. Fang, Predicting lattice thermal conductivity via machine learning: a mini review, *npj Comput. Mater.* 9 (2023) 4.
- [43] C. Verdi, F. Karsai, P. Liu, R. Jinnouchi, G. Kresse, Thermal transport and phase transitions of zirconia by on-the-fly machine-learned interatomic potentials, *npj Comput. Mater.* 7 (2021) 156.
- [44] J. Lahnsteiner, G. Kresse, J. Heinen, M. Bokdam, Finite-temperature structure of the MAPbI₃ perovskite: comparing density functional approximations and force fields to experiment, *Phys. Rev. Mater.* 2 (2018) 073604.
- [45] R. Jinnouchi, F. Karsai, G. Kresse, On-the-fly machine learning force field generation: application to melting points, *Phys. Rev. B* 100 (2019) 014105.
- [46] R. He, H. Wu, L. Zhang, X. Wang, F. Fu, S. Liu, Z. Zhong, Structural phase transitions in SrTiO₃ from deep potential molecular dynamics, *Physical Review B* 105 (2022) 064104.
- [47] J.C. Wojdel, P. Hermet, M.P. Ljungberg, P. Ghosez, J. Íñiguez, First-principles model potentials for lattice-dynamical studies: general methodology and example of application to ferroic perovskite oxides, *J. Phys. Condens. Matter* 25 (2013) 305401.
- [48] Y. Zhang, J. Zhang, X. He, J. Wang, P. Ghosez, Rare-earth control of phase transitions in infinite-layer nickelates, *PNAS Nexus* 2 (2023) 108.
- [49] J. Zhang, L. Bastogne, X. He, G. Tang, Y. Zhang, P. Ghosez, J. Wang, Structural phase transitions and dielectric properties of BaTiO₃ from a second-principles method, *Physical Review B* 108 (2023) 134117.
- [50] P. Zubko, J.C. Wojdel, M. Hadjimichael, S. Fernandez-Pena, A. Sené, I. Luk'yanchuk, J.-M. Triscone, J. Íñiguez, Negative capacitance in multidomain ferroelectric superlattices, *Nature* 534 (2016) 524–528.
- [51] M.A. Pereira Gonçalves, C. Escorihuela-Sayalero, P. Garca-Fernández, J. Junquera, J. Íñiguez, Theoretical guidelines to create and tune electric skyrmion bubbles, *Sci. Adv.* 5 (2019) eaau7023.
- [52] T. Xu, J. Zhang, T. Shimada, J. Wang, H. Yang, Intrinsic atomic-scale antiferroelectric VO₃ nanowire with ultrahigh-energy storage properties, *Nano Lett.* 23 (2023) 9080–9086.
- [53] H. Aramberri, N.S. Fedorova, J. Íñiguez, Ferroelectric/paraelectric superlattices for energy storage, *Sci. Adv.* 8 (2022) eabn4880.
- [54] G. Kresse, J. Furthmüller, Efficiency of ab-initio total energy calculations for metals and semiconductors using a plane-wave basis set, *Comput. Mater. Sci.* 6 (1996) 15–50.
- [55] G. Kresse, J. Furthmüller, Efficient iterative schemes for ab initio total-energy calculations using a plane-wave basis set, *Phys. Rev. B* 54 (1996) 11169–11186.
- [56] J.P. Perdew, A. Ruzsinszky, G.I. Csonka, O.A. Vydrov, G.E. Scuseria, L. A. Constantin, X. Zhou, K. Burke, Restoring the density-gradient expansion for exchange in solids and surfaces, *Phys. Rev. Lett.* 100 (2008) 136406.
- [57] S. Baroni, S. de Gironcoli, A. Dal Corso, P. Giannozzi, Phonons and related crystal properties from density-functional perturbation theory, *Rev. Mod. Phys.* 73 (2001) 515–562.
- [58] X. Gonze, C. Lee, Dynamical matrices, Born effective charges, dielectric permittivity tensors, and interatomic force constants from density-functional perturbation theory, *Phys. Rev. B* 55 (1997) 10355–10368.
- [59] X. Ouyang, Y. Zhuang, J. Zhang, F. Zhang, X. Jie, W. Chen, Y. Zhang, L. Liu, D. Wang, Quantum-accurate modeling of ferroelectric phase transition in perovskites from message-passing neural networks, *J. Phys. Chem. C* 127 (2023) 20890–20902.
- [60] M. Torrent, F. Jollet, F. Bottin, G. Zérah, X. Gonze, Implementation of the projector augmented-wave method in the ABINIT code: application to the study of iron under pressure, *Comput. Mater. Sci.* 42 (2008) 337–351.
- [61] X. Gonze, A brief introduction to the ABINIT software package, *Crystalline Materials* 220 (2005) 558–562.
- [62] C. Escorihuela-Sayalero, J.C. Wojdel, J. Íñiguez, Efficient systematic scheme to construct second-principles lattice dynamical models, *Phys. Rev. B* 95 (2017) 094115.
- [63] A. Togo, I. Tanaka, First principles phonon calculations in materials science, *Scripta Mater.* 108 (2015) 1–5.
- [64] A. Togo, L. Chaput, I. Tanaka, Distributions of phonon lifetimes in Brillouin zones, *Phys. Rev. B* 91 (2015) 094306.
- [65] Q. Ren, Y. Li, Y. Lun, G. Tang, J. Hong, First-principles study of the lattice thermal conductivity of the nitride perovskite LaWN₃, *Phys. Rev. B* 107 (2023) 125206.
- [66] J.M. Skelton, L.A. Burton, S.C. Parker, A. Walsh, C.-E. Kim, A. Soon, J. Buckeridge, A.A. Sokol, C.R.A. Catlow, A. Togo, I. Tanaka, Anharmonicity in the high-temperature \$Cmcm\$ phase of SnSe: soft modes and three-phonon interactions, *Phys. Rev. Lett.* 117 (2016) 075502.
- [67] G.H. Kwei, A.C. Lawson, S.J.L. Billinge, S.W. Cheong, Structures of the ferroelectric phases of barium titanate, *J. Phys. Chem. C* 97 (1993) 2368–2377.
- [68] R.A. Evarestov, A.V. Bandura, First-principles calculations on the four phases of BaTiO₃, *J. Comput. Chem.* 33 (2012) 1123–1130.
- [69] P. Ghosez, X. Gonze, J.-P.J.F. Michenaud, Lattice dynamics and ferroelectric instability of barium titanate, *Ferroelectrics* 194 (1997) 39–54.
- [70] M. Simoncelli, N. Marzari, F. Mauri, Unified theory of thermal transport in crystals and glasses, *Nat. Phys.* 15 (2019) 809–813.
- [71] J. Shieh, J.H. Yeh, Y.C. Shu, J.H. Yen, Hysteresis behaviors of barium titanate single crystals based on the operation of multiple 90° switching systems, *Mater. Sci. Eng., B* 161 (2009) 50–54.